CrossMark

ORIGINAL ARTICLE

Comprehensive preclinical evaluation of a multi-physics model of liver tumor radiofrequency ablation

Chloé Audigier[1,2] · Tommaso Mansi[2] · Hervé Delingette[1] · Saikiran Rapaka[2] ·
Tiziano Passerini[2] · Viorel Mihalef[2] · Marie-Pierre Jolly[2] · Raoul Pop[3] ·
Michele Diana[3] · Luc Soler[3,4] · Ali Kamen[2] · Dorin Comaniciu[2] ·
Nicholas Ayache[1]

Abstract

Purpose We aim at developing a framework for the validation of a subject-specific multi-physics model of liver tumor radiofrequency ablation (RFA).

Methods The RFA computation becomes subject specific after several levels of personalization: geometrical and biophysical (hemodynamics, heat transfer and an extended cellular necrosis model). We present a comprehensive experimental setup combining multimodal, pre- and postoperative anatomical and functional images, as well as the interventional monitoring of intra-operative signals: the temperature and delivered power.

Results To exploit this dataset, an efficient processing pipeline is introduced, which copes with image noise, variable resolution and anisotropy. The validation study includes twelve ablations from five healthy pig livers: a mean point-to-mesh error between predicted and actual ablation extent of 5.3 ± 3.6 mm is achieved.

Conclusion This enables an end-to-end preclinical validation framework that considers the available dataset.

✉ Chloé Audigier
chloe.audigier@inria.fr

1   Université Côte d'Azur and Inria Sophia-Antipolis
    Méditerranée Asclepios team, Inria Sophia Antipolis, France

2   Medical Imaging Technologies, Siemens Healthcare,
    Princeton, NJ, USA

3   IHU - Institut de Chirugie Guidée Par L'Image, Strasbourg,
    France

4   IRCAD - Institut de Recherche Contre Les Cancers de
    L'Appareil Digestif, Strasbourg, France

Introduction

During liver tumor radiofrequency ablation (RFA), the clinician inserts a probe percutaneously or during open surgery in the liver parenchyma, visualization of the thermal-induced necrosis progress is then unavailable. Tailoring the heating protocol to the individual patient is thus challenging due to inter-subject variability in tissue characteristics [1], the heterogeneous cooling effect of large neighboring vessels [2], porous circulation [3] and blood coagulation [4]. As a result, subject-specific computational modeling of RFA could improve the planning of the procedure and provide additional guidance during the intervention for a given patient. More specifically, such models could potentially estimate in-vivo temperatures, calculate the size, the shape and the location of the necrotic area, given the position and settings of the ablation probe in the liver. Thus, they could help the clinician in deciding where to place the heating probe and for how long heating must be applied in order to fully ablate the lesion. For instance, the probe placement has been optimized in [5] by using segmentation masks and the exploration of the set of pareto-efficient solutions.

Several approaches have been developed to describe and model RFA of liver tumors. They differ in their choice of the biophysical phenomena considered and the type of experimental data used to design and validate them. All simulations are based on the bioheat equation considering a cooling effect that is either neglected [6], spread all over the liver [4] or considering the hepatic vasculature [6–9]. The bioheat equation is simulated based on the most common discretization method: the finite element method (FEM) [6,7,10] or the

Springer

Lattice Boltzmann method (LBM) [9,11]. Other authors propose a simplified model using a weighted distance-based method [5,12] to approximate the ablation zone in real time using graphics processing units (GPU), but the analysis of the effect of an approximation instead of the complex numerical simulation has not been done yet. The cooling effect due to venous flow in the parenchyma is also considered in [8,9], whereas it is not the case for arterial flow. However, hepatic veins, portal vein and the hepatic arteries have significantly different effects on the thermal-induced lesion [13], which might be due to the difference in their flow velocities, profile and microvascular branching pattern. While the Pennes model [14] accounts for parenchymal perfusion in a simplified manner, by assuming a uniform distribution throughout the tissue, a more comprehensive model is needed to evaluate its effect. Hepatic perfusion can be simulated precisely based on micro-CT [15], but we propose an elaborated model based on vessels segmented from CT images, which does not require mesh generation, simplify the setting of boundary conditions and reduce the computational time compared to Darcy flow model for example [9].

Few authors [7–9] propose to simulate RFA on realistic subject-specific geometries extracted from images and only [11] has personalized biophysical parameters on patient data to minimize the discrepancy between simulated and measured necrotic regions. Indeed, parameters in the literature often come from tissue experiments on different species ex vivo [1], and their application to human is not granted.

Up to now, the comparison between simulated and measured necrotic regions has been used by several authors [7–9] as the main criteria of success in calculating the effect of RFA on abdominal tumors, for either model validation or personalization. However, the necrosis of tissue is the resultant of several combined physical phenomena, mainly the heat transfer and cell death mechanisms, meaning that a given ablated region may be explained by several combinations of parameters. In addition to this identifiability issue, the size of the tumor extent can only be known reliably from postoperative imaging and its shape may be highly asymmetric [1], which makes it difficult to eventually update the ablation plan during the procedure. A method that relies also on preoperative or interventional data for validation or personalization is therefore required for RFA models to be clinically useful. Those observations are complementary information to the necrotic extent for model evaluation.

Computational models of RFA depend on a large number of different parameters, which depend mostly on the patient, the temperature or the current state of the tissue. They also have a high computational cost. Understanding the observability of parameters is challenging with clinical data but is more feasible on preclinical data in a more controlled environment. This extensive validation step is important

prior to any translation into clinical settings. It is paramount because the size and the location of the RFA lesion have to be predictable and controllable for clinical applications. A comprehensive understanding of detailed multi-physics model is required first to simplify only the aspects that are not needed, which could then enable model simplification and personalization, and eventually computational models of RFA can be helpful for interventional guidance or therapy planning.

In this paper, a preclinical study for validation of RFA model is introduced, based on pre-, intra- and postoperative data ("Preclinical data acquisition and processing" section). We first present the data analysis required before using the information from the images into the model. Since our approach relies on preclinical data of healthy pigs in a controlled environment, the validation leads to an increased confidence in the computed information.

The computational model, implemented using LBM, is personalized at different levels: the anatomy is estimated from computed tomography (CT) and blood flow from phase-contrast MR imaging and invasive measurements ("Subject-specific RFA model" section). Heat transfer is computed according to the bioheat equation, coupled with a novel cellular necrosis model, equivalent to the one proposed in [16], except that we do not assume a single forward rate coefficient. A computational fluid dynamics (CFD) solver which incorporates a porous part to deal with the liver parenchyma is also used. In "Results" section, an evaluation of each preprocessing step is performed first to highlight the different sources of error. The model is evaluated on twelve ablations from five healthy pigs, inside which surrogate tumors have been implanted. Based on postoperative images and measurements, we present suitable predictions of necrotic region extent, temperature and power evolution. As we rely on a LBM implementation on GPU, a single simulation is faster than real time, which allows us to adjust key biophysical parameters. Those key model parameters (heat conductivity and heat capacity) are estimated from this pipeline by minimizing the error between the computed power and cooling temperature and the observed values. "Conclusion" section concludes the paper.

This study extends our previous work [9] on a clinical dataset of ten patients. In this work, a novel cell death model is proposed and the CFD solver used to compute the blood flow is also new. We use a complete patient-specific geometry including hepatic venous and arterial circulation systems, the addition of patient-specific boundary conditions acquired preoperatively by imaging and invasive measurements. The estimation of the main parameters of the model is performed automatically, and the evaluation of the proposed model is performed on a preclinical dataset of five pigs from a comprehensive experimental setup specially designed for RFA model validation.
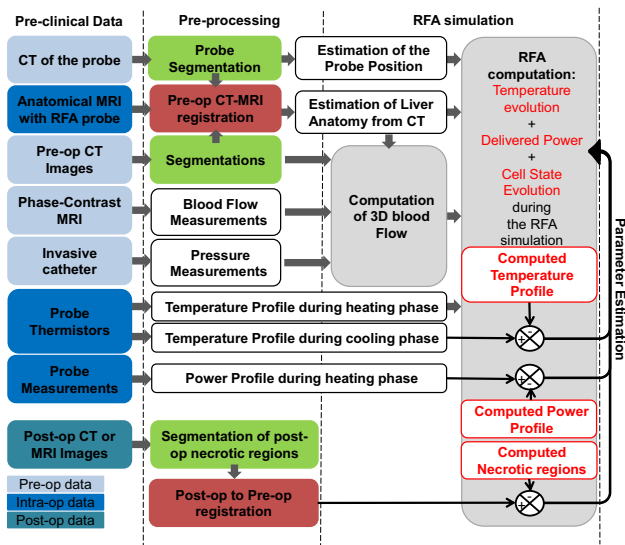
Fig. 1 Pipeline presenting the available preclinical data in *blue*, the preprocessing needed to use those data (segmentation in *green*, registration in *red*), the different computations done and finally a possible personalization framework

Fig. 2 Two CT images of Pig 1. *Left* Before surrogate tumor implantation; *Right* after surrogate tumor implantation

Preclinical data acquisition and processing

A comprehensive animal experiment has been realized specifically for model validation and parameter identification. It includes several modalities at pre-, intra- and postoperative stages. Figure 1 illustrates the available preclinical data (in blue), the different preprocessing steps needed (in red, green and white) before performing the computation (in gray).

Experimental setup

The present experimental study (No. 38.2014.01.063) received approval from the local Ethical Committee on Animal Experimentation. All animals used in the experimental laboratory were managed according to French laws for animal use and care and according to the directives of the European Community Council (2010/63/EU).

Pigs are considered as a relevant animal model as their hepatic system is similar to the human one. Several surrogate tumors (diameters <3 cm) are inserted on five swines to mimic the clinical workflow, where the clinician has to insert the RFA probe targeting the tumor and to choose its diameter depending on the tumor size. They are implanted at various locations of the liver (close to vessels or the Glisson capsule) under ultrasound (US) guidance (SIEMENS ACUSON S3000), followed by the acquisition of preoperative CT images including portal, venous and arterial phases (SIEMENS Somatom Definition A5) since it has been showed that the large vessels play an important role in the shape of the necrotic lesion [9]. The surrogate tumors
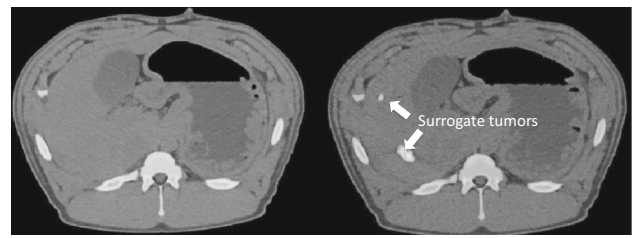
are made of a specific gel (a mix of biocompatible gelatin, alginate and nanoparticles) which exhibits a hyper-intense signal in CT and MRI as illustrated in Fig. 2. We refer to the different tumors as Pig $n - m$, for the mth tumor inserted in the nth pig. A catheter is introduced through the jugular vein to get the free and the wedge pressure in a subhepatic vein and in the vena cava. An MR compatible RFA probe, the radiofrequency interstitial tumor ablation (RITA) probe (StarBurst RFA, AngioDynamics; www.angiodynamics.com), is deployed at 2 cm of diameter (the diameter of the area defined by the tips of the probe is 2 cm) under US guidance (Fig. 3) next to the targeted surrogate tumor. An MR image is then acquired to get the position of the probe in the liver (SIEMENS Magnetom Aera 1.5T) and flow data. The temperature and delivered power are monitored (there are thermistors at the probe tips) and recorded intra-operatively during and after the ablation. Finally, to assess the extent of the necrotic areas, a postoperative CT without contrast agent to limit the radiation exposure for ethical reason, T2 or T1 + gadolinium MRI are acquired 2 days after the ablation [17–19]. Unfortunately, all the postoperative images were not systematically acquired. We would acquire as many images as possible, but depending on the pig condition, and/or the procedure duration (individual experimental changes), we were not able to acquire all the images in every case (see supplementary materials for available images). Overall, pre-, intra- and postoperative images are available, along with interventional device measurements (Fig. 1). To the best of our knowledge, no such validation setup has been reported previously in the literature.

3D modeling of the RFA probe

The geometry of the probe deployed at 2 cm is acquired from a CT image (resolution: $0.2 \times 0.2 \times 0.9$ mm) of the probe alone. A 3D mesh is then reconstructed by thresholding the image intensity (Fig. 4, left) and manually registered to the preoperative CT using the main axis of the probe and intraoperative MR data. The manual rigid registration is done
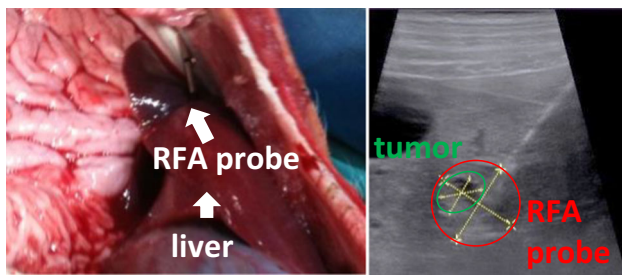
Fig. 3 *Left* Picture of the probe inside the pig liver; *Right* US image of the probe next to the surrogate tumor. The probe diameter is shown in *red*, the tumor diameter in *green*
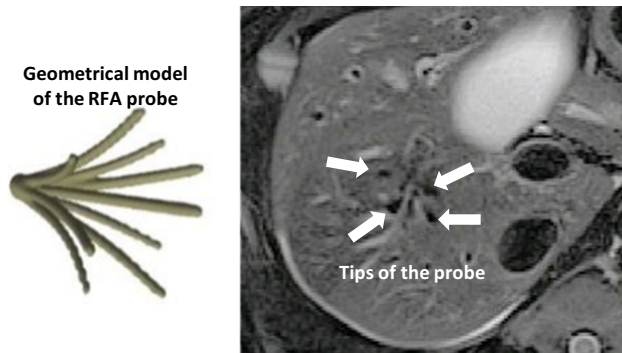

Fig. 4 *Left* Mesh model of the probe with the 9 tips derived from a CT image of the probe only; *Right* anatomical MRI with the MRI compatible probe implanted in the liver. Four tips are visible

using Paraview[1] and is visually checked by an expert up to a rotation along the probe axis. While the main axis is clearly visible as well as three or four tips (depending on the ablation considered), the MR resolution does not allow to distinguish between the nine tips of the probe individually (Fig. 4, right).

Data preprocessing: segmentation

As each structure of interest is needed as input of the RFA computational model, the segmentation of patient images is a determinant task. From the preoperative CT data, the following anatomical and pathological regions are segmented semiautomatically and meshed by the tools of Visible Patient, Strasbourg, France [20] (Fig. 5): parenchyma, hepatic veins, vena cava, portal vein, hepatic arteries and all tumors. These regions are then used to define the computational domain. The meshes are rasterized, and a multi-label mask image is created to identify the different structures on a Cartesian grid of user-defined resolution. To define the computational domain, a level set representation of the liver without tumor and vessels is computed. Necrotic areas around the surro-
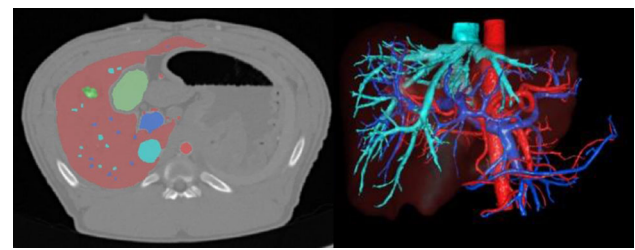
Fig. 5 Segmentation of the liver in *magenta*, arterial vessels in *red*, portal and hepatic networks in *light blue* and *dark blue*, respectively, surrogate tumors in *dark green* and gall bladder in *light green*. *Left* Overlay of the segmented areas on preoperative CT image. *Right* Vessels and liver parenchyma
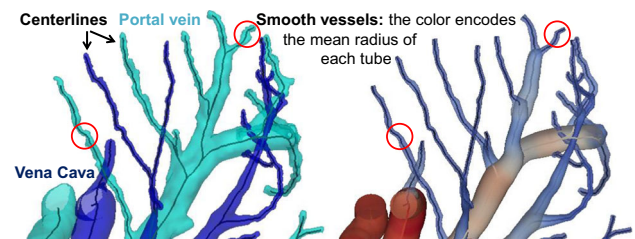

Fig. 6 *Left* Centerlines extraction from the vessel segmentation. The segmentation gives non-smooth vessels due to the anisotropy of input images. *Right* Smooth vessels generated from the centerlines

gate tumor gel are segmented and meshed from the available postoperative CT or MR data on which it is the most visible.

Data preprocessing: CFD computational domain

Smooth vessel trees The preoperative images from which the vessels are segmented have anisotropic resolution. To avoid unstable solution of the CFD solver, smooth vessel trees have to be generated from the semiautomatic segmentations. To this end, centerlines are extracted from each vessel segmentation using VMTK[2] (Fig. 6, left). Along each branch of the centerline, the mean radius is computed and the smooth vessel tree is generated by overlaying cylinders having this mean radius in a piecewise fashion (Fig. 6, right). All those cylinders are rasterized on a single image.

Blood flow from phase-contrast MRI The computational model of RFA requires as inputs the blood flow entering the vena cava, the portal vein and the hepatic artery. Instead of fixing nominal values from the literature, 2D+t phase-contrast MR images were acquired preoperatively before the probe implantation in order to impose subject-specific values as boundary conditions.

For each pig, several 2D+time sequences are acquired at different time points (9 sequences on average, min: 3, max: 17), for the reproducibility of data, and also at different locations: at the inlet of the hepatic artery, at the inlet of the
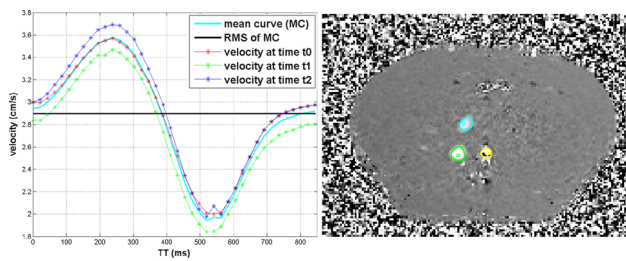
Fig. 7 *Left* Velocity in the vena cava of Pig 5 from phase-contrast MRI with respect to trigger time (all measures are registered on the cardiac pulse). In *cyan*, the mean of different measurements at different times (*red*, *blue*, *green curves*). The RMS of this curve (*black curve*) is then used as boundary conditions in the computation as φ_{vcin}. *Right* Phase-contrast MRI of Pig 5: the vena cava is segmented in *green*, the portal vein in *blue* and the aorta in *yellow*

Fig. 8 *Left* The porosity map of Pig 1 created from the vessels segmentation. The porosity is 1 in the vessels (in *white*), 0.04 in the endothelium (in *black*) and 0.1 in the parenchyma. *Right* Zoom on the porosity map. The extremities of the vessels are detected using the centerlines so that the blood flow can go through the vessel

portal vein and at the inlet of the vena cava. Given one 2D+*t* sequence, the user places a single seed in the vessel of interest in the first image and then an automatic method is used to segment this vessel on each 2D slice (Fig. 7, right) [21,22]. Using the vessel area defined by the segmentation, the mean blood flow can be computed at each time. If N 2D+*t* sequences are acquired at the same location but at different time points, this is done N times and the RMS of the mean of those N curves is used. As we learned throughout the cases how to best acquire data, we decided to use the measurements of Pig 5 for all the other cases to cope with noise, non-reproducible and non-coherent measures on the first four pigs. We assume that the values will not vary much, which is reasonable since all the pigs were healthy, of similar weight and age. For Pig 5 (vena cava), the acquisition has been done at three different time points ($N = 3$). The RMS of the mean of those three curves is used (Fig. 7, left black curve) since numerical results have shown that pulsatile velocity profile in large blood vessels has little difference in effect on the thermal lesion region of tissue compared with uniform or parabolic velocity profile [23].

Pressure from invasive measurements The computational model of RFA requires also vena cava and hepatic artery blood pressures as inputs (see arrows in Fig. 9 for the locations where the boundary conditions are applied). In order to impose subject-specific values as boundary conditions, these blood pressures have been measured to avoid the use of nominal values from the literature. The pressures at the outlet of the vena cava and the hepatic artery were measured invasively by catheter introduced through the jugular vein. The same values (from Pig 5) are used as boundary conditions in the five pigs, as it is the case for the blood flow measurements.

Porosity map The porosity, defined as the fraction of blood volume (V_{b}) over the total volume (V_{t}): $\epsilon = V_{\text{b}}/V_{\text{t}}$, has to be defined everywhere in the computational domain as it is an input of the CFD solver. The vessel walls are defined as follow. The smooth vessel trees are rasterized on a single image. On this image, we perform a 26-connexity dilation on

the voxels of the vessels to model the endothelium and avoid the flow to go through the vessel wall. The extremities are detected using the centerlines previously used, and the porosity at the extremities is set to the parenchyma porosity value. Figure 8 shows an example of porosity map. The porosity value is 1 in the CT visible vessels, 0.1 in the parenchyma [8], modeled then as a porous medium. Experiments have been performed to obtain a sufficiently small porosity (0.04) in the vessel walls (impermeable medium) to avoid the occurrence of shear stress on the vessel walls (leakage) [11].

Data preprocessing: post-to-pre registration

Due to ethical reasons, CT with contrast agent could not be acquired 2 days after intervention, making accurate post- to preoperative registration challenging. In order to compare the results of the computation with the ground truth given by the postoperative images, registration of the post- to the preoperative image is performed. For each pig, the preoperative image (CT from different phases) does not necessarily belong to the same modality as the postoperative image (CT or MRI (T2 or T1 + gad)) due to individual experimental changes. Moreover, the pigs are in neither a similar position nor a similar condition, as they had an empty stomach the day of the intervention, which was not true 2 days after. Breathing has also an important impact on the shape of the liver. For those reasons, we choose to register the postoperative meshes to the preoperative image instead of pure image-to-image registration. From the semiautomatic segmentation of the postoperative image, a tetrahedral mesh is generated using CGAL.[3] From the segmentation of the preoperative image, a binary mask of the liver including vessels and arteries is gen-

---

[3] www.cgal.org.

erated. Using the SOFA framework,[4] the postoperative mesh is deformed elastically to match the intensity profile in the preoperative image using the finite element method (FEM) and a corotational model [24]. First-order implicit Euler time integration is employed, and the system of equation is solved with the conjugate gradient algorithm. The computed deformation field is then applied to the necrotic surface mesh using a barycentric mapping between the coordinates of the surface mesh and the tetrahedral mesh (12,000 tetrahedra and 3000 nodes for Pig 5). The registration is fast to perform; it took 178 s on a Windows 7 laptop machine (Intel Core, 2.40 GHz, 8 GB RAM, 8 CPUs) on average to register the postoperative mesh to the preoperative image.

Subject-specific RFA model

Liver blood flow computation

Model description We want to get simultaneously the blood flow in the large visible venous and arterial vessels, as well as in the parenchyma. To that end, the flow in the main vessels and in the parenchyma is simultaneously calculated using the generalized 3D incompressible Navier–Stokes equation for fluid flow in porous media [25]. More precisely, writing $\mathbf{v}$ as the blood velocity and p the pressure inside the liver, we solve:

$$\frac{\partial \mathbf{v}}{\partial t} + \mathbf{v} \cdot \nabla \mathbf{v} = -\frac{1}{\rho_b}\nabla p + \frac{\mu}{\rho_b}\nabla^2 \cdot \mathbf{v} \underbrace{- \frac{\mu(1-\epsilon)^2}{\alpha^2 \epsilon^2}\mathbf{v}}_{\mathbf{F}} \qquad (1)$$

The last term of Eq. (1) is the added force $\mathbf{F}$ that models the total body force due to the presence of a porous medium [26]. $\mathbf{F}$ depends on the porosity ϵ (fraction of blood volume over the total volume) defined through a porosity map (Fig. 8) as described in the previous section. ρ_b is the blood density, μ, the shear viscosity of the fluid and α^2 an effective parameter.

Boundary conditions At the border of the liver, no flux boundary conditions are used (Neumann), whereas Dirichlet boundary conditions are applied at the inlets and at the outlet of the large vessels: The portal vein, vena cava and arterial inflows, φ_p, $\varphi_{vc_{in}}$ and φ_a are given from preoperative phase-contrast MR images, whereas the vena cava and arterial outlet pressures p_0 and p_a are given from catheterization. Figure 9 illustrates boundary conditions on a subject-specific geometry.

This method makes the boundary conditions simple to treat: No boundary conditions are fixed on the extremities of the vessels inside the parenchyma thanks to the use of the porosity map, contrary to [9].
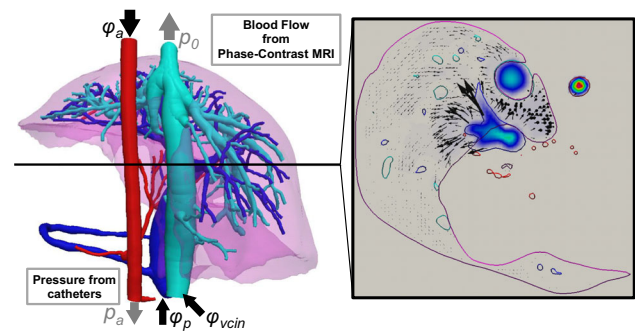
---

[4] http://www.sofa-framework.org.

Fig. 9 *Left* Model of the hepatic circulatory system. *Black* (resp. *gray*) *arrows* denote blood flow (resp. outlet pressures) which are fixed as boundary conditions. *Right* Slice showing the computed blood flow in the vessels and parenchyma. The velocity magnitude is color coded, and the velocity vectors are shown in *black* in the parenchyma

Numerical computation using LBM Equation (1) is solved using the Lattice Boltzmann Method (LBM) for fast computation on general purpose graphics processing units (GPU). LBM has been developed for CFD and is now a well-established discretization method [27]. In this paper, LBM is used to compute the porous and blood flow circulation in the liver. To this end, an isotropic Cartesian grid with 19-connectivity topology is used (D3Q19 scheme defined in Fig. 10, left) as well as a multiple-relaxation-time (MRT) model, for increased stability [28]. At position $\mathbf{x}$ for the edge $\mathbf{e}_i$ of the grid, the governing equation is:

$$\mathbf{f}(\mathbf{x} + \mathbf{e}_i\Delta x, t + \Delta t) = \mathbf{f}(\mathbf{x}, t) + \mathbf{A}[\mathbf{f}^{eq}(\mathbf{x}, t) - \mathbf{f}(\mathbf{x}, t)]$$
$$+ \Delta t \mathbf{g}(\mathbf{x}, t)$$
$$f_i^{eq}(\mathbf{x}, t) = \omega_i \rho_b [1 + \frac{\mathbf{e_i}.\mathbf{v}}{cc_s^2}]$$
$$g_i(\mathbf{x}, t) = \omega_i \rho_b \frac{\mathbf{e_i}.\mathbf{F}}{c_s^2}$$

In this equation, $\mathbf{f}(\mathbf{x}) = \{f_i(\mathbf{x})\}_{i=0...18}$ is the vector of distribution function with $f_i(\mathbf{x})$ being the probability of finding a particle traveling along the edge $\mathbf{e}_i$ of the node $\mathbf{x}$ at a given time; $c = \Delta x/\Delta t$; $c_s^2 = 1/3$; Δx is the spacing; $\boldsymbol{\omega} = \{\omega_i\}_{i=0...18}$ is the vector of weighting factors and $\mathbf{A}$ the MRT matrix. The fluid mass density and velocity are computed from the LBM distributions as $\rho_b = \sum_{i=0}^{18} f_i(\mathbf{x}, t)$ and $\rho_b\mathbf{v} = \sum_{i=0}^{18} \mathbf{e}_i f_i(\mathbf{x}, t) + \rho_b\mathbf{F}\Delta t/2$ and are updated at every node of the grid for every time step Δt.

Heat transfer and cellular necrosis models

Heat transfer model The coupled bioheat equation describes how the heat flows from the probe through the liver while taking into account the cooling effect of the blood flow [29]. It depends on the patient-specific anatomy (the segmentation process was presented in
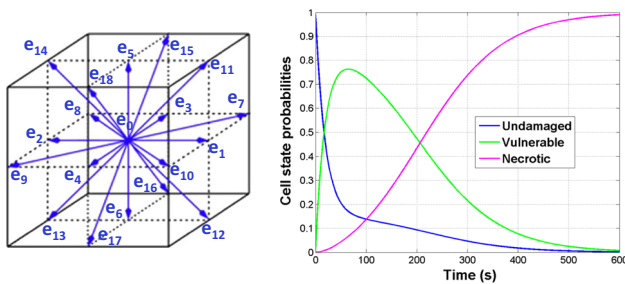
Fig. 10 *Left* D3Q19 scheme used in the LBM computation of the blood flow. *Right* Cell-state evolution over time when tissue is heated at 105 °C during 10 min

"Data preprocessing: segmentation" section) and on the blood flow inside the main vessels and the parenchyma considered as a porous medium.

It has be shown [29] analytically and computationally but in 1D that the coupled bioheat equations can be simplified into the Pennes model [14] in the case of large vessels, and into the WK model in the case of small vessels. Therefore, the temperature T is computed by solving the following equations, either a reaction-diffusion or an advection-diffusion equation:

$$\rho_t c_t \frac{\partial T}{\partial t} = Q + \nabla \cdot (d_t \nabla T) \begin{cases} +R(T_{b0} - T) \\ -\alpha_v \rho_b c_b \mathbf{v} \cdot \nabla T \end{cases} \tag{2}$$

where ρ, c, d are the density, heat capacity, conductivity; subscripts t and b stand for tissue and blood, respectively. Q is the source term, α_v, the advection coefficient, R, the reaction coefficient (it corresponds to $H/(1 - \epsilon)$ from [8]) and T_{b0} the blood temperature (assumed constant) in large vessels. In this case, the advection is the transport mechanism of the heat by the blood due to its motion, whereas the diffusion is the transport mechanism due to a temperature difference within a same region but without any motion. The Pennes Model is solved in the large visible vessels and the WK model in the liver parenchyma. Our model includes the heat sink effect of all hepatic vessels (veins and arteries) as well as the effect of the blood flow within the parenchyma considered as a porous medium.

A weak coupling is considered: The blood flow has an influence on the temperature distribution through the advection term in the WK model and through the reaction term in the Pennes model but the temperature does not affect the blood flow (coagulation is not considered here), which allows us to speed up the calculations since the blood flow distribution is computed only once, at the beginning of the simulation, and is run until a steady state is reached.

Cellular necrosis model A three-state model [30] is coupled with the bioheat equation to compute tissue necrosis. Each cell has a probability to be either undamaged (U), vulnerable

(V) or necrotic (N). Those probabilities vary with the temperature spatially and temporally according to the following transition diagram:

$$[U] \; \underset{\gamma}{\overset{\beta(T)}{\rightleftarrows}} \; [V] \; \overset{\delta(T)}{\longrightarrow} \; [N]$$
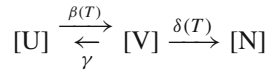
where $\beta(T) = \bar{\beta} e^{T/T_k}$, $\delta(T) = \alpha\beta(T)$ and γ are the transition rates. Unlike in [16], a constant α is introduced ($\alpha = \bar{\delta}/\bar{\beta}(1 + 10N)$) to decouple the damage rate from the vulnerable rate coefficient, so that three distinct transition rates are considered to allow cells to reach the vulnerable state. This diagram results in three coupled ODEs (Eq. 3), solved with a first-order explicit scheme on the same grid and with the same time step as the bioheat equation.

$$\begin{cases} \dfrac{dU}{dt} = -\beta(T)U + \gamma V \\ \dfrac{dV}{dt} = \beta(T)U - (\gamma + \delta(T))V \\ \dfrac{dN}{dt} = \delta(T)V \end{cases} \tag{3}$$

The property: $U + V + N = 1$ is also imposed at each point. Figure 10 (right) represents the solution of Eq. (3) at one vertex over time if a constant temperature of 105 °C is applied.

For both heat transfer and cell death models, parameters are initially set to values from the literature [8] reported in Table 1, assumed similar for surrogate tumor and hepatic tissue.

The cell death model is strongly coupled to the bioheat equation as the heat capacity depends on the state of the cell (c_t^U, c_t^V and c_t^N correspond, respectively, to the heat capacity of undamaged, vulnerable and necrotic tissue) and the conductivity d_t depends on the temperature through $d_t = \bar{d}_t * (1 + 1.61 * (T - 310) \times 10^{-3})$ as in [8]. All the remaining parameters are constant.

Numerical computation using LBM Eq. (2) is also solved using LBM with a MRT model. In RFA, it has been used to compute heat transfer and validated through a comparison with an analytical solution [9], for a similar accuracy as FEM, though it has the advantage to be easily parallelized in GPU.

An isotropic Cartesian grid with 7-connectivity topology has been found sufficient [9]. Neumann conditions at the liver boundary defined as a level set function are applied. For a time step of $\Delta t = 0.5$ s and a spatial resolution of $\Delta x = 0.5$ mm, better than real-time computation can be achieved on a desktop machine (Windows 7, Intel Xeon, 3.30 GHz, 16 GB RAM, 12 CPUs, Nvidia Quadro K5000 4.0 GB). For example, it took around 10 min to compute 17 min of ablation of Pig 4-1.

Table 1 Nominal parameter values from the literature [8]

Notation	Parameter name	Nominal
T_k (°C)	Parameter of cell death model	40.5
$\bar{\beta}$ (s^{-1})	Damage rate coefficient	3.3×10^{-3}
γ (s^{-1})	Recovery rate coefficient	7.7×10^{-3}
$\bar{\delta}$ (s^{-1})	Vulnerable rate coefficient	3.3×10^{-3}
c_t^V (J(kg K)$^{-1}$)	Heat capacity of vulnerable tissue	3.6×10^3
c_t^N (J(kg K)$^{-1}$)	Heat capacity of necrotic tissue	0.67×10^3
c_t^U (J(kg K)$^{-1}$)	Heat capacity of undamaged tissue	3.6×10^3
$\bar{d}_t$ (W(m K)$^{-1}$)	Heat conductivity	0.512
R (W(m^3 K)$^{-1}$)	Reaction coefficient	27.1×10^4
α_v	Advection coefficient	0.11

Heating power and cooling temperature computation

We assume that the equilibrium between probe and tissue temperature is reached. During the heating period, a Dirichlet boundary condition is used to fix the temperature at the point sources of the probe tips: RFA is simulated by imposing as input the temperatures measured at the five thermistors in a small neighborhood around the probe tips: a layer of several voxels, thus simulating the source term Q from Eq. (2). The four remaining tip temperatures are linearly interpolated from these values. Imposing temperature values does not prevent of observing large temperature gradient next to the tips. This large gradient of temperature is in fact observed in our simulations. The heating stops at time $t = t_a$. During this period ($t < t_a$), the heating power can be computed, whereas the cooling temperature can be computed when ($t > t_a$).

Heating stage We assume that the measured power is strongly correlated (proportional) to the heat power $P(t)$ delivered through radio frequency to heat the liver tissue. Proportionality is assumed to account for power dissipation due to electrical resistance, and the unknown surface ratio of the probe being heated, but also since we do not model the heat loss by Joule effect. The heat power $P(t)$ delivered to the tissue can be computed at each time step of the simulation from the bioheat equation according to Fourier's law:

$$P(t) = \alpha \int_S d_t \frac{\partial T(t)}{\partial \mathbf{n}} dS \qquad (4)$$

S is the probe surface, $\mathbf{n}$ is the outer normal at that surface and α, the proportionality coefficient ($\alpha = 0.4469$), found by matching the peak value of the measured power for Pig 1-1 with the peak value of the simulated power with personalized parameters. This value is then used in all the computations.

Cooling stage In the absence of any delivered heat power, the nine tips of the probe cool down at a speed which depends on the local conductivity d_t and the heat capacity c_t. Thus,

during the cooling period $t_c - t_a$ (cooling stops at time $t = t_c$), the cooling temperature can be simulated.

Parameter estimation from probe measurements

During the intervention, the delivered power and the temperature distribution are measured by the ablation probe itself. We explore how these information can be used to estimate apparent values of some model parameters. During the heating phase, the simulated heat power P_s can be compared to the measured one P_m. During the cooling phase, the simulated temperatures $\mathbf{T_s}$ can be compared with the measurements $\mathbf{T_m}$ read from five tips of the probe (four tips do not have any thermistors).

In this study, the nominal parameters in the heat transfer and cellular necrosis equation come from the literature. After a non-reported sensitivity analysis, we choose to estimate apparent values of the heat capacity c_t^U and the constant part of the conductivity $\bar{d}_t$ as they mainly influence the delivered power, the temperature distribution and the size of ablated regions. As temperature maps are not readily available, these two apparent values of the parameters are obtained by minimizing the following cost function:

$$\arg\min_{c_t^U, \bar{d}_t} \left(\frac{1}{t_a} \sum_{t=0}^{t=t_a-\Delta t_m} \frac{(P_m(t) - P_s(t))^2}{\sigma_{P_m}^2} \right.$$
$$\left. + \frac{1}{t_c - t_a} \sum_{t=t_a}^{t_c} \frac{(m_{T_m}(t) - m_{T_s}(t))^2}{\sigma_{T_m}^2} \right) \qquad (5)$$

Δt_m is the measurement time step; σ_{P_m} and σ_{T_m} are the standard deviations associated with the heat power and the temperature, both of them evaluated from the variability in the available observations and equal to 13.3 W and 5.1 °C in our experiments. σ_{P_m} acts as a normalization factor in Eq. (5). It is computed from the twelve ablations at one time point during the heating phase ($t = 50$ s), time at which all power curves are coherent (Fig. 11).
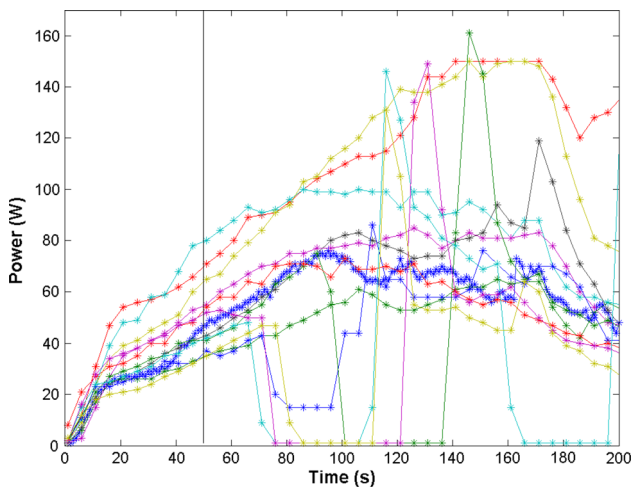
Fig. 11 *Plot* of the 12 delivered power curves for the first 200 s. The mean and standard deviation are computed at $t = 50$ s. This time is a good compromise since it is not too early, avoiding the boundary condition effect, and not too late, before the cell death could affect the delivered power. The wild fluctuations are due to the different heating/cooling phases

$\sigma_{T\,\mathrm{m}}$ is computed from the 5 temperature curves extracted from the cooling phase of one ablation (Pig 1-1), where all the temperature curves are coherent. We did not use all the twelve ablations as their cooling stage did not start at the same time. It is defined as follow:

$$\sigma_{T\,\mathrm{m}}^2 = \frac{1}{t_\mathrm{c}} \sum_{t=t_\mathrm{a}}^{t=t_\mathrm{c}} \left(\frac{1}{5} \sum_{i=1}^{5} (T_i(t) - m_T(t))^2 \right)$$

$$m_T(t) = \frac{1}{5} \sum_{i=1}^{5} T_i(t)$$

To cope with the uncertainty in the rotation of the probe along its axis, the mean tip temperature $m_T(t)$ is used for the personalization instead of directly mapping the tip temperatures.

Results

Evaluation of the preprocessing

Evaluation of the registration The accuracy of the registration is visually checked by an expert (Fig. 12). Whenever available, the non-rigid transformation is applied to the postoperative vessel and/or tumor meshes and they are compared to their preoperative equivalent meshes. Point-to-mesh errors from pre- to registered postoperative meshes are computed for Pig 2 (Table 2). Before the non-rigid registration, all the meshes are centered. The error is decreased after the registration except for tumor 1 where the two meshes are already in good agreement before the registration.

Fig. 12 *Left* Superposition of the postoperative mesh model in *red* on the preoperative binary image; *Right* comparison between the registered postoperative vessel meshes in *red* (portal vein in thick, vena cava in *thin lines*) and the preoperative ones

Table 2 Point-to-mesh errors from the pre- to the postoperative meshes in millimeter before and after the registration for Pig 2

Mesh	Before registration	After registration
Hepatic veins	4.53 ± 2.13	2.30 ± 0.97
Portal vein	6.13 ± 3.81	4.88 ± 4.38
Arteries	21.34 ± 23.25	17.60 ± 19.71
Tumor 1	2.25 ± 1.38	2.80 ± 1.49
Tumor 2	8.80 ± 6.51	5.28 ± 4.50
Liver	6.91 ± 3.57	3.53 ± 1.60

Before the registration, all the meshes are centered

Table 3 Dice, positive predictive value (PPV) and sensitivity between the original and the smoothed vessel images for Pig 4

Mesh	DICE (%)	PPV (%)	Sensitivity (%)
Arteries	93.1	93.9	92.3
Portal vein	91.3	85.3	98.3
Hepatic veins	84.9	93.8	77.5

Evaluation of the smooth vessels trees In order to evaluate the creation of the smooth vessels trees, DICE, positive predictive value (PPV) and sensitivity scores between the original and the smoothed vessel images are computed for Pig 4 (Table 3). They show a good correlation between the original segmented vessels and the generated ones.

Verification of the CFD solver on a synthetic case A cylindrical mesh with spherical inlet and outlet (Fig. 13) is used to validate the CFD solver in the case of a porous medium. Blood flow is set at the inlet and pressure at the outlet. The flow entering the vessel Φ_in should entirely go out: $\Phi_\mathrm{in} = \Phi_\mathrm{out}$, in the case of a single vessel (case 1: Fig. 13, left) but also in the case where the flow crosses a porous medium, a porosity map is used to emulate two veins and
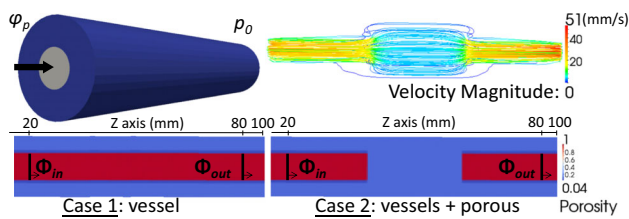
Fig. 13 Synthetic case used to validate the CFD solver. *Top left* A cylindrical mesh with spherical inlet and outlet is used. The boundary conditions are the inflow and the outlet pressure. *Top right* The velocity field given by the CFD solver in the second case. *Bottom row* The porosity field used in the two cases
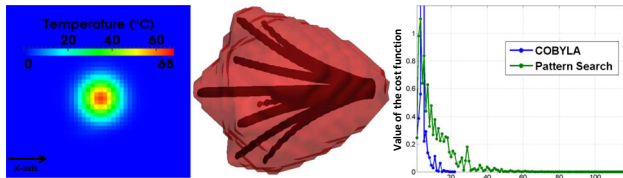

Fig. 14 *Left* Setup of the synthetic case: the temperature map around one tip of the probe, and the necrotic area (*red*) created around the probe (*dark*). *Right* Convergence curves of the COBYLA algorithm (*blue*) and of the pattern search algorithm (*green*). The cost function is shown with respect to the number of iterations

the liver parenchyma (case 2: Fig. 13, right). The porosity is set to 1 inside the vessels, 0.04 in the endothelium and 0.1 outside. The mass conservation is verified by comparing the flow through the surface of the "vessel" at $z = 20$ mm: Φ_{in} and at $z = 80$ mm: Φ_{out}. In both cases, a difference between these two fluxes of 3% is achieved.

Verification of the parameter estimation framework

As illustrated in Fig. 1, the framework enables parameter estimation too.

Synthetic data generation In order to verify the parameter estimation framework, we consider a synthetic case on a simplified regular cuboid domain, to speed up the process (Fig. 14, left). As we try to estimate the heat conductivity and the heat capacity, the advection is not considered here.

We apply the typical clinical RFA protocol: During 3 min, the temperature is increased linearly at the tips of the probe to reach 105 °C and then maintained for 6 min. Finally, a cooling stage is observed (no temperature imposed) for three more minutes. The extent of the necrotic area, delivered power and temperature during the cooling stage are simulated and then used as ground truth to estimate the parameters: $\bar{d}_t$ and c_t by minimizing the cost function (Eq. 5).

Comparison of optimization methods We compare two gradient-free optimization methods available in DAKOTA[5]:

[5] http://dakota.sandia.gov—multilevel framework for sensitivity analysis.

the Constrained Optimization BY Linear Approximations (COBYLA) and the pattern search method (PS). Those methods are sequential trust-region algorithms; therefore, they do not rely on initial values, but explore the whole domain of parameters in a first stage. The range of parameters values used [7] are reported in Table 4, and the other parameters are fixed to the nominal values (Table 1).

First, a ground truth is considered using the values of c_t and $\bar{d}_t$ found in "Discussion" section corresponding to healthy swine tissue. Using COBYLA, we estimate the parameters with 0.8% error on $\bar{d}_t$ and 0.6% on c_t in 30 min after 22 iterations with a cost function value of 7.8×10^{-5} and a mean of the symmetric point-to-mesh error of 10^{-4} mm. Similarly, using PS, we manage to obtain the estimated parameters with 0.4% of error on $\bar{d}_t$, 0.3% on c_t in 154 min after 117 iterations with a cost function value of 7.2×10^{-6} and a similar mean of the symmetric point-to-mesh error of 10^{-4} mm. The convergence curves of both optimizations are shown in Fig. 14 (right). We choose the COBYLA method to perform the personalization as it requires less iterations of the forward model to estimate the parameters with similar accuracy as PS.

Evaluation Cirrhotic tissue behaves like a thermal insulator, preventing to heat outside the tumor targeted for the ablation, leading to the so-called oven effect [31]. In order to mimic this effect, the heat conductivity is divided by two (to the best of our knowledge, no value are reported in the literature) to generate the ground truth, which differs from the one obtained with the nominal value (Fig. 15, right). We manage to find the correct cirrhotic value of $\bar{d}_t$ (Fig. 15, left).

We verified on a synthetic case, that our method allows to find "cirrhotic" value of the heat conductivity in the case of a diseased liver in the absence of noise and model error.

Evaluation on swine data

We now evaluate our method on the available swine data, whose liver tissues are healthy.

During our experiments, the measured electrical power appears consistently to reach its maximum during the increase in temperature, before the plateau of 105 °C (Fig. 16, left) in all cases. Given the considered model and the Fourier's law used to compute the delivered power (Eq. 4), this phenomena cannot be explained by a constant heat capacity which would lead to a peak after the plateau is reached. Instead, following a non-reported sensitivity analysis, we propose to adapt the necrosis model of [16], so that the cells reach their vulnerable state faster, which is one way to explain this observation. By modifying $\bar{\delta}$, the two forward transitions $[U] \rightarrow [V]$ and $[V] \rightarrow [N]$ are decoupled so that tissues

Table 4 Ranges of parameters values explored in the optimization framework

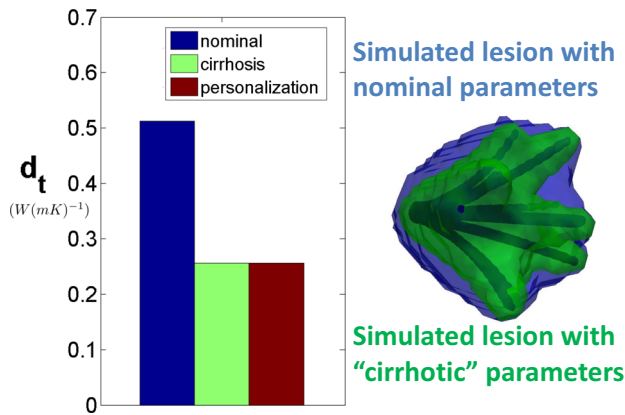| Notation	Parameter name	Min	Max
c_t^U J(kg K)$^{-1}$	Heat capacity of undamaged tissue	18	54
$\bar{d}_t$ W(m K)$^{-1}$	Heat conductivity	0.256	0.768

Fig. 15 *Left* The parameter estimation framework leads to the correct "cirrhotic" value of $\bar{d}_t$. *Right* The lesion obtained with the "cirrhotic" $\bar{d}_t$ in *green* is enclosed within the lesion obtained with the nominal value in *blue*
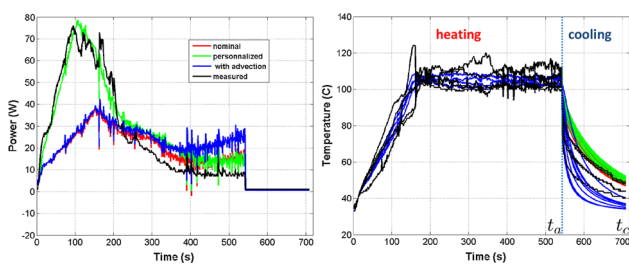

Fig. 16 Temperature and delivered power evolution for Pig 1-1. 3 different computations: with nominal parameters (*green curves*), personalized parameters (*red curves*), and with advection (*blue curves*) are compared with actual measurements (*black curves*). *Left* The error on the power evolution computed over the heating phase is reduced from 19.9 to 7.5 W after personalization and stays constant with advection (20.8 W). *Right* The error on the temperature evolution computed over the cooling phase is reduced from 10.3 to 9.7 °C with the advection, but stays constant after personalization (11.1 °C). The advection clearly affects the temperature evolution

can reach very quickly their vulnerable state which entails a significant change of c_t (Table 5).

The model is evaluated on twelve ablations performed on five swines (some swines have several surrogate tumors). While the large and CT visible hepatic vessels have a cooling effect affecting the shape of the thermal lesion [13], the effect of the hepatic perfusion due to the small vessels non-visible on CT images has not been clearly identified so far. For this reason, the simulations are performed without the advection term, capturing the hepatic perfusion, except in "Effect of the advection" section in order to understand
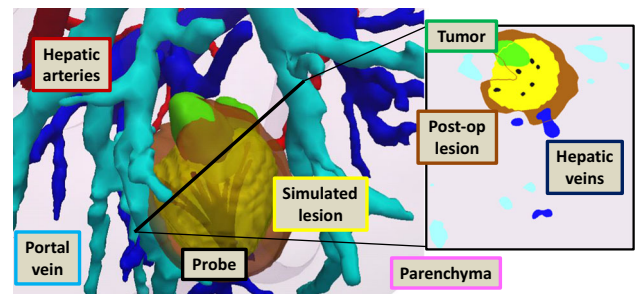

Fig. 17 *Left* The simulated lesion in yellow is showed around the RFA probe in the subject-specific geometry on Pig 4-2. *Right* A single orthogonal slice shows that the simulated lesion is qualitatively close to the registered postoperative lesion in brown: point-to-mesh error of 4.6 ± 3.9 mm. The *color of the boxes* correspond to the *color* of the respective regions

its effect on the necrotic lesion. By keeping the reaction term, we only consider the heat sink effect of the blood on the large visible vessels in each simulation. The applied RFA protocol is not exactly the same for all ablations. Eight ablations are performed through several short cooling and heating periods, whereas the other four ablations included only one long final cooling stage after a continuous heating period. For all pigs, nominal values of parameters (Table 1) are employed. In each case, the simulated lesion is compared to the ground truth. Figure 17 shows results for Pig 4-2.

Quantitatively, symmetric point-to-mesh errors implemented like in [32] computed between the simulated lesion and the registered postoperative ground truth show suitable prediction of the necrotic extent (in red in Fig. 18): average over all ablations of 5.3 ± 3.6 mm of mean point-to-mesh error, smaller than the targeted surrogate lesions diameter (around 2–3 cm), which can be considered as sufficient for clinical applications. Similarity scores averaged over all ablations are as follows: DICE: 44%, sensitivity: 47% and PPV: 53% (in red in Fig. 19). We achieve errors of 26 W and 5.1 °C on average between measured and simulated values of cooling temperature and delivered power (in red in Fig. 20), which is good compared to the targeted ablation temperature of 105 °C and the maximal power of 150 W.

Parameter personalization

COBYLA is used to minimize the cost function (Eq. 5) as only a few forward simulations (typically 20) are required.
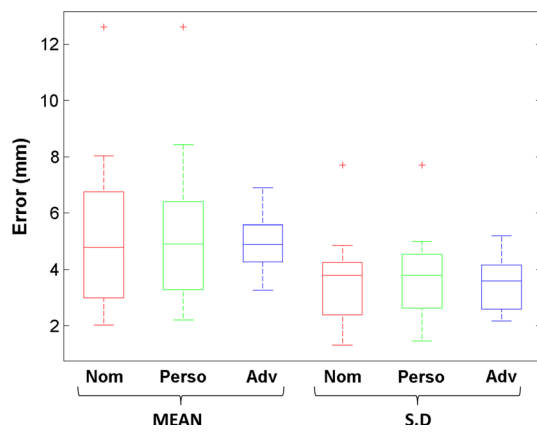
Fig. 18 Results for three different computations: with nominal parameters, with personalized parameters and with the advection term. For the computation with the advection term, only 6 ablations are considered. Mean and standard deviation of the point-to-mesh in mm computed on the surface of the lesion
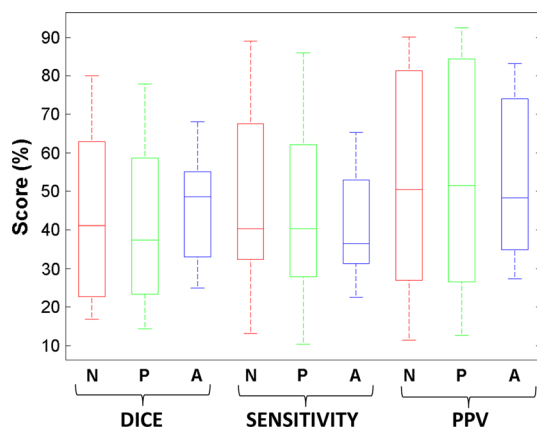

Fig. 20 *Left* Error computed during the heating phase on the power in W. *Right* Error computed during the cooling phase on the temperature in °C

Fig. 19 Similarity scores (DICE, sensitivity and positive predictive value) in % computed on the volume of the lesion

As the data originate from healthy pigs of similar age and weight, we hypothesize that their parameters would be similar too. The vulnerable rate coefficient is also adjusted to match the raise in delivered power as detailed in "Evaluation on swine data" section. The minimization of the error between measured and simulated values of power and temperature is done only on two tumors with a long final cooling stage (2 different Pigs: Pig 1-1 and Pig 4-3) as it is long enough to observe reliably the effect of the conductivity $\bar{d}_t$, yielding two sets of personalized values. The values independently found on the two swines are really close: The same value of heat capacity c_t^U is estimated, and the conductivity values are almost equal to the nominal value as expected (Table 5). The estimated parameters are then used on the ten remaining cases to evaluate the discrepancy in terms of temperature, delivered power and necrotic area. Small errors were obtained in those cases too, without previously having fit the parameters for those tumors. On average,
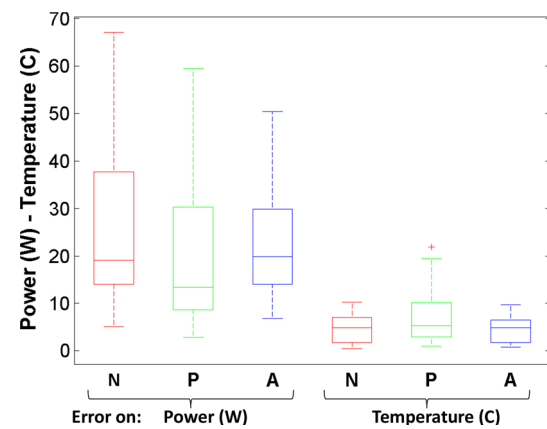
the temperature and power errors are 7.8 °C and 20.4 W (in green in Fig. 20), the mean of the point-to-mesh error is 6.0 mm (in green in Fig. 18), and similarity scores are DICE: 42%, sensitivity: 43%, PPV: 55% as illustrated in green in Fig. 19. Qualitatively, as shown in Fig. 21 (green curves), the simulated heat power and temperature are close to the heat power and the temperature given by the RFA probe itself. On average, the error is reduced after the use of personalized parameters: from 35 to 30 W and from 5.9 to 1.9 °C. It is mainly reduced on the first heating period (from 50 W to 27 W). During the cooling phase, the simulated (non-imposed) temperature is compared to the measured one, whenever measurement is available (the RFA power was turned off during some cooling phases).

Effect of the advection

To quantify the effect of hepatic perfusion, the simulations are performed by adding the advection term for all pigs whenever it is possible to segment the vena cava inlet (not possible for Pig 2 and 4). On average, the effect of the advection cannot be clearly highlighted. The mean of the point-to-mesh error over the 6 ablations computed with advection is 5.0 ± 3.5 mm (in blue in Fig. 18), the average similarity scores are: Dice: 46%, sensitivity: 42% and PPV: 53% (in blue in Fig. 19). On average, the error on the simulated power is 22 W and 4.7 °C on the temperature (in blue in Fig. 20). Those values are comparable to the values obtained without the advection term. As shown in Fig. 21 (blue curves), the errors remain constant with the advection term (35 W and 6.3 °C). In some cases, the advection reduces the error in term of necrotic extent and temperature distribution (Pig 5-1), but not always (Pig 1-1). The advection term always changes the shape of the necrotic extent (Fig. 22).

Table 5 Comparisons between personalized and nominal values of estimated parameters

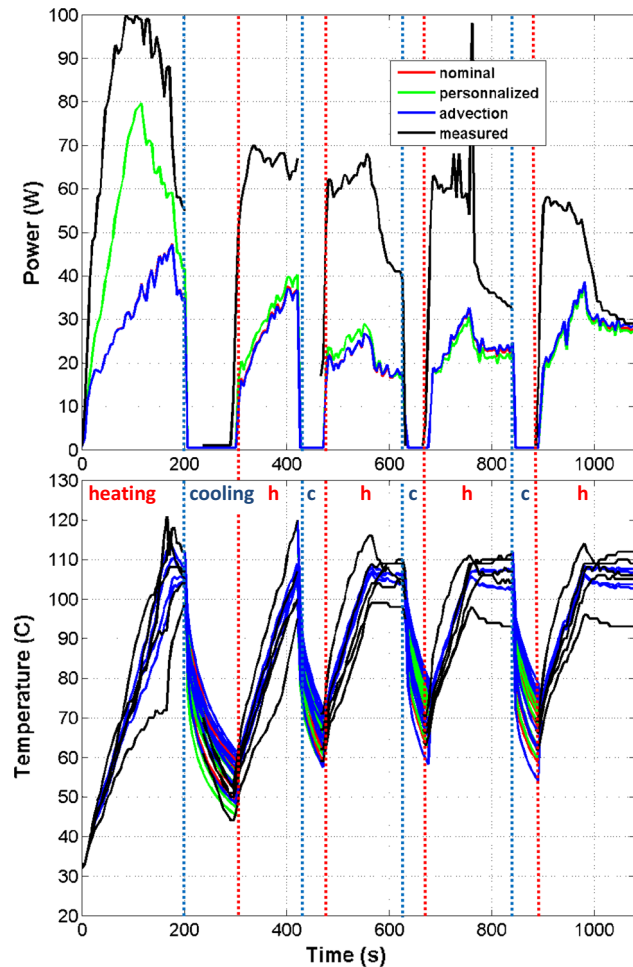| Notation	Nominal value	Personalized on Pig 1-1	Values on Pig 4-3	Automatic optimization
$\bar{\delta}$	3.3×10^{-3}	1×10^{-4}	1×10^{-4}	No
c_t^{U}	3.6×10^{3}	3.6×10^{1}	3.6×10^{1}	Yes
$\bar{d}_t$	0.512	0.614	0.512	Yes

Fig. 21 Temperature and delivered power evolution for Pig 3-1. 3 different computations: with nominal parameters (*green curves*), personalized parameters (*red curves*), and with advection (*blue curves*) are compared with actual measurements (*black curves*). During the heating phase, the temperature is imposed: 5 temperatures are directly imposed from the 5 thermistors measurements (superposition of *blue* and *black curves*) and the 4 remaining temperatures are imposed from a linear interpolation from those measurements (*four blue curves*). The red curves are really similar to the *blue curves*, and they can hardly be distinguished

Fig. 22 Comparison between the simulated and the postoperative necrotic areas on Pig 1-1. *Left* The post-op lesion is showed around the RFA probe in the subject-specific geometry. *Right* Single slice showing the simulated lesions with (*gray*) and without (*yellow*) advection compared to the registered postoperative lesion (*brown*). The advection has an effect on the shape of the lesion; however, in this case, it does not improve the point-to-mesh error: 6.9 ± 5.2 mm versus 4.8 ± 4.4 mm. The *box colors* correspond to the *color* of the regions

Effect of the registration

One important part of the validation is the comparison of the simulated necrotic extent with a lesion segmented on a postoperative image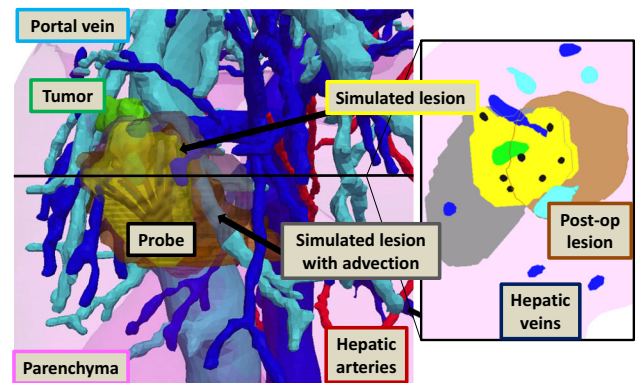 registered to the preoperative image. The modality of the postoperative image is not always the same (CT or MR). The resolution and the size of the postoperative image do not always allow an accurate registration of the lesion, as for Pig 2-2 (resolution: $0.78 \times 0.78 \times 4.8$ mm, size: $384 \times 384 \times 36$ mm). To check the sensitivity of the computation to the registration, a new algorithm is used for this tumor only. We rigidly translate the postoperative lesion so that the barycenter of the postoperative lesion coincides with the barycenter of the simulated necrotic extent (Fig. 23, right). With this simple registration method, the results are significantly improved. The lesion registration strongly affects the error measured between the computed necrotic area and the ground truth.

Effect of the probe position

The position of the probe is known from an intra-operative MRI. In some cases, the probe artifact and the image contrast do not allow an accurate registration, as for Pig 3-2. A new computation is performed for this tumor to check the sensitivity of the computation to the probe position. The same configuration is used except that we manually put the probe inside the registered postoperative lesion (position 2 in Fig. 24).
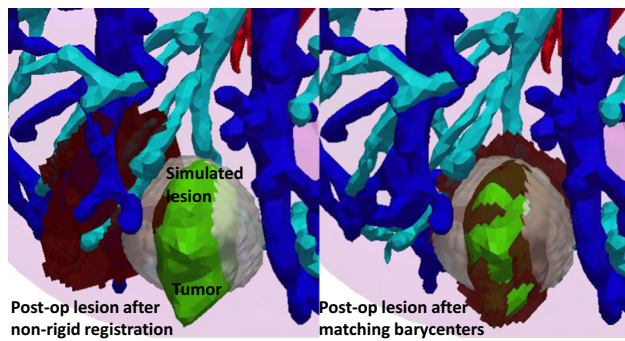
Fig. 23 Effect of the registration on Pig 2. *Left* The postoperative lesion after the non-rigid registration is showed in the subject-specific geometry. The point-to-mesh error is 8.4 ± 5.0 mm. *Right* The post-op lesion after matching barycenters. The point-to-mesh error reduces to 3.6 ± 2.9 mm
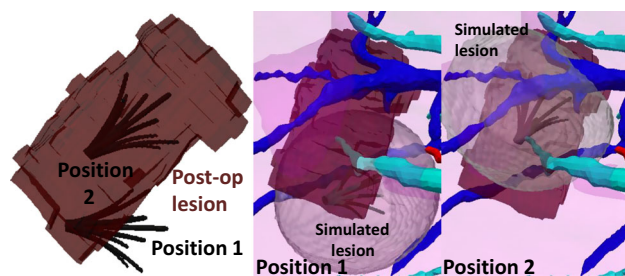

Fig. 24 *Left* The postoperative lesion is showed around 2 possible positions for the RFA probe on Pig 3-2. *Right* Zoom on the ablation area, the simulated lesion is closer to the registered postoperative lesion when the probe is in position 2, point-to-mesh error of 6.2 ± 4.0 mm versus 12.6 ± 7.7 mm in position 1

With this probe position, the results are significantly improved. The probe position affects the error measured between the computed necrotic area and the ground truth (Fig. 24). It is equivalent to a registration error since by moving the probe, we move the computed necrosis.

Discussion

We presented a first quantitative evaluation of RFA computation, which combines a multi-physics model and multimodal medical images from a preclinical study. Despite possible biases in the probe location and in establishing correspondences from the post- to the preoperative images due to registration errors, our model provided new insights.

Model limitations

The proposed model has several limitations. We assume that tumor and healthy hepatic tissue have similar properties. Experiments could be performed to assess the effect of different spatial properties on the resulting necrosis. The measured
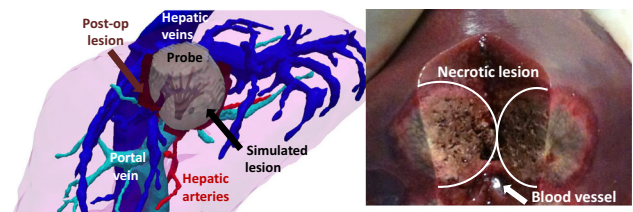

Fig. 25 *Left* The simulated necrotic extent around the RFA probe, close to the border of the liver from Pig 3-3. The postoperative lesion is shown in *brown*. *Right* The liver extraction confirms that the necrotic lesion is subcapsular

power is assumed to be proportional to the power delivered through radio frequency. The Neumann boundary condition (no heat transfer through the liver surface) may not be valid. If the ablation location is subcapsular (Pig 5-1, 4-1, 3-3), the volume of the simulated ablation becomes larger, as the heat bounces back on the border and increases artificially the heat diffusion inside the liver (Fig. 25). However, the liver has a high regulation capacity thanks to its rich vascular system. If the heat is applied close to the liver border, it is not clear how it dissipates, whether or not it will affect the neighboring organs. Moreover, the weak coupling between the heat transfer model and the CFD model does not allow to consider coagulation or the cessation of perfusion at temperature above 60 °C, which is known to have a major impact on ablation lesion size. However, this type of coupling due to coagulation has not been modeled so far by any research team. Finally, during the RFA computation, the temperature at the tips of the probe is imposed. It would be more accurate to directly impose the delivered power as in [33] and thus simulate the cooling as well as the heating temperature distribution. This requires to solve the spatiotemporal electromagnetic heating problem, adding more complexity to the model, whose impact on the final thermal output is questionable and difficult to validate. Moreover, this raises some technical issues as Neumann instead of Dirichlet boundary condition would have to be applied.

Effect of the registration

After several trials of registration algorithms, we were able to reliably estimate in some cases, the deformation between pre- and postoperative imaging to evaluate the necrosis extent prediction. But the registration method uses only the liver surface, and two lesions are poorly registered. However, by taking the hepatic vessels into account as well, the registration could be improved. It should also be noted that the registration method differs from the one in [34], where the necrotic lesions were registered rigidly to the preoperative image by aligning its barycenters which could introduce bias in the analysis. The impact of those registration processes has been evaluated on one tumor in this paper.

Toward personalization

In clinical settings, due to the large variety of liver conditions found during RFA (cirrhosis, fibrosis, etc.), we cannot assume inter-patient invariance of the biophysical parameters, as done here for the five pigs. Parameter personalization is then required, and the proposed method may be suitable to get subject-specific parameters from easily accessible intra-operative quantities (the probe temperature and delivered power). We proposed a biophysical computational model whose computing time, although already shorter than the real physical process, remains too long to allow an easy use in a well-established clinical workflow. But an extensive evaluation of such a comprehensive model is needed before simplifications are made to reduce its complexity and the invasive input data. The proposed method could then be translated into clinical practice, as several heating/cooling phases are generally necessary to perform a complete ablation. The first heating/cooling phase could be used to personalize the main parameters of the model, which could then give a patient-specific prediction of the lesion. Such a framework could help the clinician during the intervention: The probe position could be improved and/or the heating duration could be adjusted if the simulated lesion does not cover entirely the tumor for example. We evaluated the discrepancy in terms of temperature and delivered power, and we showed that key parameters can be estimated. This is a proof of concept not only for the ability to personalize the model but also for its predictive power by evaluating the simulation results on ten different tumors.

The necrotic extent is mainly controlled by the conductivity $\bar{d}_t$ and the heat capacity of vulnerable cells c_t^{V} (not c_t^{U}). $\bar{d}_t$ was not changed after optimization, so no significant difference in terms of necrotic area (mean of the point-to-mesh error: 6.0 vs 5.3 mm on average) or cooling temperature (error: 7.8 vs 5.1 °C) appeared after personalization, despite a better match for the power (error: 20.4 vs 25.9 W) as illustrated in Fig. 16. Moreover, the point-to-mesh errors were of the order of 5 mm; it suggests that simulations with optimized $\bar{d}_t$ and c_t^{U} might be realistic in terms of necrotic area, power and temperature predictions.

The novel approach leads to an estimation of temperature away from the probe at any time during the ablation without requiring any information about the necrotic regions. This additional information could be used as surrogate to assess the amount and location of damaged tissue during the intervention (cells receiving excessive heat but without being necrosed) surrounding the ablated region. Furthermore, as the probe temperature and delivered power are available, in real-time, from the RF system, they could therefore be used for therapy guidance, provided that heat transfer can be computed much faster than real-time.

Preclinical study challenges

The preclinical validation approach was difficult to establish. It involves surrogate tumors implantation to mimic the RFA current clinical practice; however, the surrogate tumors do not have any blood perfusion, and we assumed that they have tissue properties similar to hepatic tissue. It required acquisitions of different modalities (CT, MRI, US), at different times (pre-, intra- and postoperative images). The different images at Day 1 (day of intervention) should be acquired quickly, as the anesthesia of the pig cannot last too long since the pig will be kept alive for 2 additional days. Due to the high complexity of the experimental setup, preprocessing is necessary. The segmentation was performed semiautomatically, but the vessel meshes had to be smoothed to avoid unstable solution of the CFD solver. The probe was segmented from a CT image with a good resolution, but the artifacts induced by the probe and the bad resolution of the interventional MR images did not allow to accurately register the probe position. The setting of subject-specific boundary conditions for the blood flow and pressure was not straightforward, since the acquisition process of phase-contrast MR images was complex to handle and requires a significant learning curve. Due to the non-reproducible and non-coherent measures on the first four pigs, the measures of blood flows and pressures of Pig 5 only were used in all the computations.

Despite a comprehensive model and a complete preclinical study for its validation, many sources of errors are involved at the modeling level, but also at each preprocessing step. We are not able to accurately locate the position where the pressure was measured, but we assume that there is no variation in pressure in a small neighborhood of the two outlets. Even if the impact of the segmentation process has to be taken into account, we managed to identify most of the errors thanks to the preclinical study. In a clinical setup, the use of an invasive catheter to measure the pressure is not possible, neither the acquisition of phase-contrast MRI, intra-operative MRI with the probe, injected CT with the three different phases, which are not part of the standard clinical workflow for RFA. Even if many of the patient-specific parameters used in this study would not be precisely available for each patient, this work is a first step forward to get an insight on the most sensitive parameters to be personalized and those which do not affect the final output. A comprehensive biophysical model is therefore required for this evaluation. However, with a simplified blood flow model for example, those measurements will not be required. Mathematical models can improve the current clinical practice by providing more information to the clinician for the guidance but also for the planning of the procedure. However, the questions of validation and error in the predictions of such computational models are often neglected, whereas it is absolutely key to their potential clinical use. Having a model as detailed as

possible is important to fully evaluate the effects of the different biophysical phenomena involved, and it is paramount to identify the sources of errors. A study of the errors is a necessary next step before using model-based therapy in clinical routine. Knowing how the preprocessing errors (due to segmentation, vessels smoothing, post-to-pre or probe registration) propagate to the final computational outcome would be of great interest. It would help to understand the modeling errors and to be more confident on the resulting ablation. The validation could be improved by acquiring images of better resolution, but this would impact the well-being of animals in the current framework.

Conclusion

In this paper, we presented a sophisticated preclinical setup to validate a complete multi-physics model of RFA. This comprehensive validation was based on pre-, intra-, postoperative images and device-based measurements. The RFA computational model relies on LBM and takes into account the main biophysical phenomena (heat transfer, cellular necrosis, hepatic blood flow). The advection effect of the porous circulation [11] is considered by including a CFD model, robust to image noise and anisotropy to compute the venous and arterial blood flow in the liver parenchyma. We also showed that parameter estimation is possible to reduce the bias introduced by the use of nominal parameters. The approach was successfully evaluated on twelve ablations from five swines, opening new opportunities for RFA planning and guidance.

Compliance with ethical standards

Conflict of interest The authors declare that they have no conflict of interest.

Ethical approval All procedures performed in studies involving animals were in accordance with the ethical standards of the institution or practice at which the studies were conducted.

Informed consent This articles does not contain patient data.

References

1. Hall SK, Ooi EH, Payne SJ (2015) Cell death, perfusion and electrical parameters are critical in models of hepatic radiofrequency ablation. Int J Hyperth 31(5):538

2. Patterson EJ, Scudamore CH, Owen DA, Nagy AG, Buczkowski AK (1998) Radiofrequency ablation of porcine liver in vivo: effects of blood flow and treatment time on lesion size. Ann Surg 227(4):559

3. Crezee J, Lagendijk J (1990) Experimental verification of bioheat transfer theories: measurement of temperature profiles around large artificial vessels in perfused tissue. Phys Med Biol 35(7):905

4. Chang IA, Nguyen UD (2004) Thermal modeling of lesion growth with radiofrequency ablation devices. Biomed Eng Online 3(1):27

5. Schumann C, Rieder C, Haase S, Teichert K, Süss P, Isfort P, Bruners P, Preusser T (2015) Interactive multi-criteria planning for radiofrequency ablation. Int J Comput Assist Radiol Surg 10:1–11

6. Jiang Y, Mulier S, Chong W, Diel Rambo M, Chen F, Marchal G, Ni Y (2010) Formulation of 3D finite elements for hepatic radiofrequency ablation. Int J Modell Identif Control 9(3):225

7. Altrogge I, Preusser T, Kroger T, Haase S, Patz T, Kirby RM (2012) Sensitivity analysis for the optimization of radiofrequency ablation in the presence of material parameter uncertainty. Int J Uncertain Quantif 2(3):295–321

8. Payne S, Flanagan R, Pollari M, Alhonnoro T, Bost C, O'Neill D, Peng T, Stiegler P (2011) Image-based multi-scale modelling and validation of radio-frequency ablation in liver tumours. Philos Trans R Soc A 369(1954):4233

9. Audigier C, Mansi T, Delingette H, Rapaka S, Mihalef V, Boctor E, Choti M, Kamen A, Ayache N, Comaniciu D (2015) Efficient lattice Boltzmann solver for patient-specific radiofrequency ablation of hepatic tumors. IEEE Trans Med Imaging 34(7):1576

10. Chen X, Saidel GM (2009) Mathematical modeling of thermal ablation in tissue surrounding a large vessel. J Biomech 131:5–24

11. Audigier C, Mansi T, Delingette H, Rapaka S, Mihalef V, Carnegie D, Boctor E, Choti M, Kamen A, Comaniciu D, Ayache N, (2014) Lattice-Boltzmann method for fast patient-specific simulation of liver tumor ablation from CT images. In: MICCAI workshop ABDI

12. Rieder C, Kroeger T, Schumann C, Hahn HK (2011) GPU-based real-time approximation of the ablation zone for radiofrequency ablation. Trans Vis Comput Gr 17(12):1812

13. Frericks BB, Ritz JP, Albrecht T, Valdeig S, Schenk A, Wolf KJ, Lehmann K (2008) Influence of intrahepatic vessels on volume and shape of percutaneous thermal ablation zones: in vivo evaluation in a porcine model. Investig Radiol 43(4):211

14. Pennes HH (1998) Analysis of tissue and arterial blood temperatures in the resting human forearm. J Appl Physiol 85(1):5

15. Schwen LO, Krauss M, Niederalt C, Gremse F, Kiessling F, Schenk A, Preusser T, Kuepfer L (2014) Spatio-temporal simulation of first pass drug perfusion in the liver. PLoS Comput Biol 10(3):e1003499

16. ONeill D, Peng T, Stiegler P, Mayrhauser U, Koestenbauer S, Tscheliessnigg K, Payne S (2011) A three-state mathematical model of hyperthermic cell death. Ann Biomed Eng 39:570

17. Goldberg SN, Gazelle GS, Compton CC, Mueller PR, Tanabe KK (2000) Treatment of intrahepatic malignancy with radiofrequency ablation. Cancer 88(11):2452

18. Lardo AC, McVeigh ER, Jumrussirikul P, Berger RD, Calkins H, Lima J, Halperin HR (2000) Visualization and temporal/spatial characterization of cardiac radiofrequency ablation lesions using magnetic resonance imaging. Circulation 102(6):698

19. Dickfeld T, Kato R, Zviman M, Nazarian S, Dong J, Ashikaga H, Lardo AC, Berger RD, Calkins H, Halperin H (2007) Characterization of acute and subacute radiofrequency ablation lesions with nonenhanced magnetic resonance imaging. Heart Rhythm 4(2):208

20. Soler L, Nicolau S, Pessaux P, Mutter D, Marescaux J (2014) Characterization of acute and subacute radiofrequency ablation lesions with nonenhanced magnetic resonance imaging. Hepatobiliary Surg Nutr. 3(2):73

21. Gulsun MA, Tek H (2006) 3D modeling of coronary arteries. In: MICCAI workshop CVII

22. Guetter C, Xue H, Chefd'Hotel C, Guehring J (2011) Efficient symmetric and inverse-consistent deformable registration through interleaved optimization. In: IEEE international symposium on biomedical imaging: from nano to macro. IEEE, pp 590–593

23. Horng TL, Lin WL, Liauh CT, Shih TC (2007) Effects of pulsatile blood flow in large vessels on thermal dose distribution during thermal therapy. Med Phys 34(4):1312

24. Faure F, Duriez C, Delingette H, Allard J, Gilles B, Marchesseau S, Talbot H, Courtecuisse H, Bousquet G, Peterlik I, Cotin S, (2012) Sofa: a multi-model framework for interactive physical simulation. In: Soft tissue biomechanical modeling for computer assisted surgery. Springer, pp 283–321

25. Nithiarasu P, Seetharamu K, Sundararajan T (1997) Natural convective heat transfer in a fluid saturated variable porosity medium. Int J Heat Mass Transf 40(16):3955

26. Guo Z, Zhao T (2002) Lattice-Boltzmann model for incompressible flows through porous media. Phys Rev E 66(3):036304

27. Chen S, Doolen GD (1998) Lattice Boltzmann method for fluid flows. Ann Rev Fluid Mech 30(1):329

28. Pan C, Luo LS, Miller CT (2006) An evaluation of Lattice Boltzmann schemes for porous medium flow simulation. Comput Fluids 35(8):898

29. Peng T, ONeill D, Payne S (2011) A two-equation coupled system for determination of liver tissue temperature during thermal ablation. Int J Heat Mass Transf 54(9):2100

30. Breen M, Chen X, Wilson D, Saidel, (2002) Modeling cellular thermal damage from radio-frequency ablation. In :EMBS/BMES conference, vol 1. IEEE, p 715

31. Livraghi T, Goldberg SN, Lazzaroni S, Meloni F, Solbiati L, Gazelle GS (1999) Small hepatocellular carcinoma: treatment with radio-frequency ablation versus ethanol injection. Radiology 210(3):655

32. Zheng Y, Barbu A, Georgescu B, Scheuering M, Comaniciu D (2007) Fast automatic heart chamber segmentation from 3D CT data using marginal space learning and steerable features. In: ICCV. IEEE, pp 1–8

33. Kröger T, Altrogge I, Preusser T, Pereira PL, Schmidt D, Weihusen A, Peitgen HO (2006) Numerical simulation of radio frequency ablation with state dependent material parameters in three space dimensions. In: International conference on medical image computing and computer-assisted intervention. Springer, pp 380–388

34. Audigier C, Mansi T, Delingette H, Rapaka S, Mihalef V, Pop R, Diana M, Soler L, Kamen A, Comaniciu D, Ayache N (2015) Challenges to validate multi-physics model of liver tumor radiofrequency ablation from pre-clinical data. In: MICCAI workshop on computational biomechanics for medicine X